JOURNAL OF SYNCHROTRON RADIATION

ISSN 1600-5775

Received 10 October 2018
Accepted 3 December 2018

Edited by M. Yabashi, RIKEN SPring-8 Center, Japan

[1] This article will form part of a virtual special issue on X-ray free-electron lasers.

Keywords: undulator systems; beam-based alignment; radiation damage; phase shifters; quadrupole movers; high-duty-cycle machines.

First operation of the SASE1 undulator system of the European X-ray Free-Electron Laser[1]

S. Abeghyan,[a] M. Bagha-Shanjani,[a] G. Chen,[b] U. Englisch,[a] S. Karabekyan,[a] Y. Li,[a] F. Preisskorn,[a] F. Wolff-Fabris,[a] M. Wuenschel,[a] M. Yakopov[a] and J. Pflueger[a]*

[a]European XFEL, Holzkoppel 4, 22869 Schenefeld, Germany, and [b]Institute of Fluid Physics, Chinese Academy of Engineering Physics, 64 Mianshan Road, Mianyang, 62199, People's Republic of China.
*Correspondence e-mail: joachim.pflueger@xfel.eu

The European XFEL comprises three undulator systems. All of the systems use standardized mechanical, magnetic and control components. The key elements such as undulators, phase shifters and quadrupole movers as well as their controls are described, with special emphasis on the SASE1 undulator system, which was the first to become operational and has been lasing since May 2017. The role of these systems for the commissioning is outlined with special emphasis on beam-based alignment, which was important to achieve first lasing. Radiation damage was observed. The exposure doses were measured with the online radiation dosimetry system. Countermeasures and latest results are reported, which are important for a high-duty-cycle machine such as the European XFEL.

1. Introduction

At the European XFEL (EuXFEL), the FEL radiation is generated in three gap-tuneable undulator systems called SASE1, SASE2 and SASE3. Since the electron-beam energy of the EuXFEL is variable between 8.5 and 17.5 GeV, a combination with gap variation allows for a change in the radiation wavelength from 0.05 to 0.4 nm for SASE1 and SASE2 with a period length of 40 mm and from 0.4 to 5.2 nm for SASE3 with a period length of 68 mm. Table 1 gives an overview of the parameters of the three EuXFEL undulator systems. On SASE1, first lasing was observed in May 2017 and user operation started in September 2017. Meanwhile, lasing was obtained on the other two systems as well. However, this contribution concentrates on SASE1.

2. Undulator system overview

Some aspects of the EuXFEL undulator systems have already been outlined in several publications (Altarelli *et al.*, 2006; Pflueger *et al.*, 2013; Li, Abeghyan *et al.*, 2015). In order to allow for economical manufacturing, all components are strictly standardized. State-of-the-art planar permanent-magnet hybrid technology based on neodymium iron boron (NdFeB) magnets and soft iron poles made of cobalt iron is used for the magnet structures. In view of the high duty cycle of 27000 bunches s^{-1} specified for EuXFEL, the free aperture of the vacuum chamber was conservatively chosen to be 8.6 mm × 15 mm (vertical × horizontal) allowing for a minimum magnetic gap of the undulators of 10 mm. All undulators are 5 m long and use identical standard mechanical drive and support systems. In order to safely reach saturation

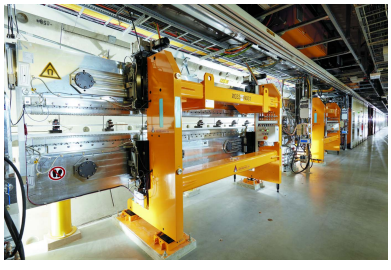

Table 1
Specifications for the undulator segments of the EuXFEL.

The operational ranges for gap and K parameter match user requirements (Altarelli *et al.*, 2006). Only inside are all specifications strictly fulfilled. Magnetic tuning was always performed at the tuning gap to limit gap dependence of magnetic properties, see discussion of Fig. 4.

	SASE1 / SASE2	SASE3
Undulator type	U40	U68
Period length (mm)	40	68
Segment length (m)	5	5
Total number of poles	248	146
Magnetically active poles	246	144
Number of ending poles	3	3
Operational gap range (mm)	10–20	10–25
Operational K-parameter range	1.65–3.9	4–9
Maximum peak field @ 10 mm (T)	1.11	1.66
Tuning gap (mm)	14	16
Maximum gap (mm)	200	200
Maximum phase jitter (°)	≤8	≤8
Maximum 1st B_y field integral (T mm)	±0.15	±0.15
Maximum 1st B_x field integral (T mm)	±0.15	±0.15
RMS of 2nd B_y integral (T mm^2)	<100	<210
RMS of 2nd B_x integral (T mm^2)	<100	<100
Radiation wavelength range (nm)	0.05–0.4	0.4–5.2
Number of segments in system	35	21
System length (m)	205	121

at the shortest wavelengths, long undulator systems are needed, which are formed by combining cells. One is shown in Fig. 1. Parameters of the undulator systems are given in Table 1.

Each cell of the EuXFEL consists of a 5 m-long undulator segment and a 1.1 m-long intersection, which comprises the following components: a quadrupole for beam focusing; a quadrupole mover with a horizontal/vertical movement range of ±1.5 mm for beam steering (Munilla *et al.*, 2011, 2015); a phase shifter (Lu *et al.*, 2009), which matches the optical phase of the radiation field with micro-bunched electron beam; a cavity-beam-position monitor (BPM) with sub-micrometre resolution (Lipka *et al.*, 2016); and two horizontal/vertical air coil correctors (Pflueger & Pannier, 2009), one on either end to compensate steering errors of the undulator. Fig. 2 shows a downstream view along the SASE1 system after installation in the tunnel. The heavy hardware explained in Fig. 1 is installed on the tunnel floor, while the light cabinets for the electronics of the control systems are mounted about 2.5 m above, underneath the ceiling next to the supporting trays for cooling water pipes. The whole undulator system is hermetically encased in an enclosure. It has walls which can be easily opened and removed if needed. It completely separates its internal air flow from the rest of the tunnel. This enclosure is seen in the rear of Fig. 2, where its walls are kept closed. In the front they are opened and removed for access. An air conditioning system located on the downstream end of the enclosure provides an air flow of 15000 m^3 h^{-1}. It stabilizes the undulator system locally better than ±0.1°C over 24 h. Along the undulator system, a slight but very stable temperature gradient of about −1.4°C is permitted going from the downstream to upstream end. Temperature variation can be compensated by slightly retuning the gaps of the undulator segments as a function of their local temperatures. This compensation is optional. If it is turned on, the local temperatures are measured with an accuracy better than ±0.1°C at a rate of 10 Hz. The gaps are corrected only occasionally if this limit is exceeded. The correction coefficient for the temperature correction is slightly gap dependent and varies in the operational gap range (10–20 mm) from 11.5 to 12.7 µm °C^{-1} (Pflueger, 2012).

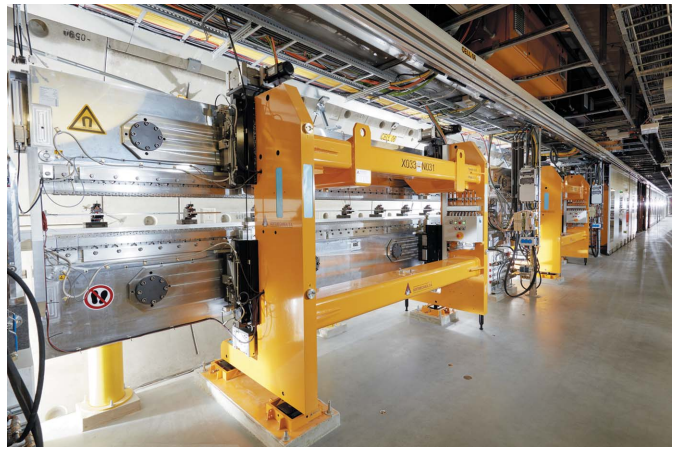

Figure 2
Downstream view along the SASE1 undulator system during installation. The walls for the temperature stabilized enclosure are normally in place and closed as seen in the rear. In the front they are temporally removed for access.

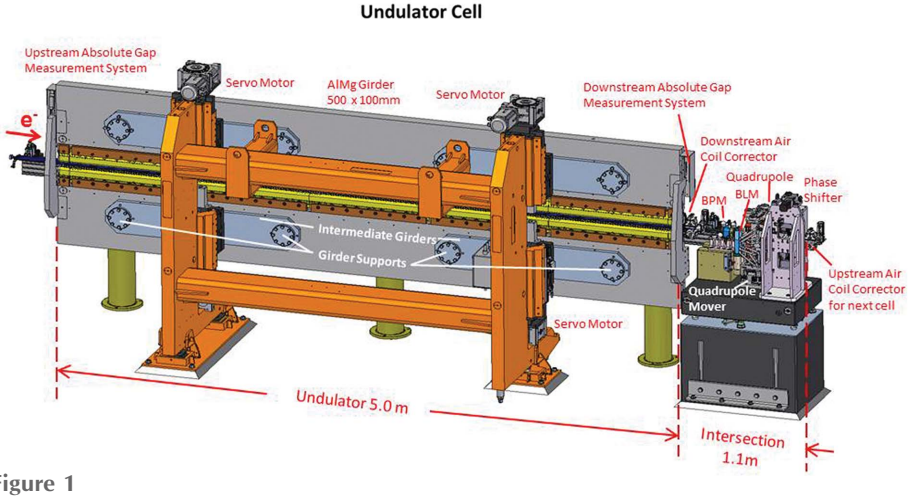

Figure 1
Representative cell of the undulator systems of the EuXFEL

A short description of the principal hardware elements of the undulator system is given below.

2.1. Undulator segments

An undulator segment installed in the SASE1 undulator system is

shown in Fig. 2. The gap is opened to about 100 mm so that the supports of the vacuum chamber can be seen. This facilitates the exchange of undulators without breaking the vacuum. The undulator vacuum chambers are made from aluminium–magnesium (Al–Mg) extrusions. In combination with machining, an inner horizontal/vertical aperture of 8.6 mm × 15 mm and an outer chamber thickness of 9.6 mm is obtained. This allows us to reliably obtain the specified minimum magnetic gaps of 10 mm (Dommach *et al.*, 2018). A standard undulator segment, as shown in Fig. 1, consists of a massive frame made of steel, which supports the linear guides for the four gap drive units. Each consists of a servo motor, a high reduction gear, and a planetary roller spindle, and acts on an intermediate girder made of non-magnetic stainless steel. Each provides two supports for the two 5 m-long non-magnetic girders made of Al–Mg alloy with a cross section of 500 mm × 100 mm. In this way, there is a fourfold support of each girder, which substantially reduces the deformation under magnetic forces of up to 17 tons. The gap is measured directly with two absolute linear encoder systems, one on each end, with a verified accuracy of ±1 µm. The four servo motors are electronically synchronized to allow for accurate gap motion with this accuracy. The girders have a standardized interface profile so that they can be used for both the SASE1 and SASE3 magnet structures. Magnets and poles are mounted in 0.9 m-long modules made of the same Al–Mg alloy as the girders to avoid any thermal deformation effects by differential expansion. They provide a stable body for magnets and poles and are attached to the girders using clamps.

For the exact tuning of magnetic properties, pole height tuning (PHT) was further refined and developed (Pflueger *et al.*, 1999; Li, Abeghyan *et al.*, 2015). For PHT, exact magnetic measurements at the so-called tuning gap are a precondition. This gap was selected empirically at 14 mm to minimize gap dependence, see discussion below. In a first step the local K parameters of each pole and its correction to the average are calculated. In a second step the required pole shifts for each pole are calculated and executed. After this step a homogeneous distribution of the local K parameters is obtained, which results in very low phase errors, see below (Li, Abeghyan *et al.*, 2015).

The principle of the mechanical pole adjustment is shown in Fig. 3(*a*). A pole is positioned by four screws. The screws on the gap side are used for adjustment, while those on the back side are used for fixation. Fig. 3(*b*) shows one undulator during tuning. The gap is fully opened and the tuning device using four digital dial indicators is inserted and used to control pole adjustment to an accuracy of ±1 µm. Vertical field errors are tuned by adjusting the local gap of a pole, which can be adjusted by up to ±300 µm but is limited to ±100 µm to avoid limitation of the minimum gap. Horizontal field errors are tuned by tilting poles by up to ±4 mrad. This method requires no shims and the magnetic specifications as shown in Table 1 could be fulfilled for about 95% of the undulators. Only in a very few cases do shims need to be applied (Li, Ketenoglu & Pflueger, 2015).

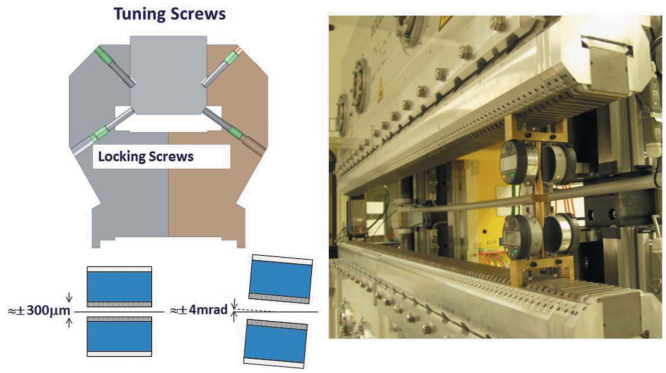

(*a*) (*b*)

Figure 3
(*a*) Principle of pole height tuning. Each pole is kept in place by four screws. The tuning screws allow for vertical movement of up to ±0.3 mm and a tilt of up to ±4 mrad. The locking screws are tightened afterwards with a specified torque to secure the adjustment. (*b*) Measurement bridge for precision measurement of pole shift and tilt. Top and bottom poles are adjusted simultaneously using two digital dial gauges for each, with a resolution of 1 µm.

Air coil correctors are used at either end of an undulator, see Fig. 1. They are an integral part of the undulator and are controlled dynamically by its control system using lookup tables. Their purpose is to set the proper correction currents at any gap so that there is no deflection or excursion of the beam in that undulator segment. The use of the air coils offers three advantages: (1) the specifications for gap-dependent steering errors of the end sections on first field integrals of the permanent magnet part of the structure can be released significantly to ±0.150 T mm; this reduces tuning time. (2) The total first and second field integral of an undulator can be kept to zero for any gap. (3) The correction can be changed any time during operation by updating the lookup tables for example if electron-beam-based measurements are made.

Fig. 4 shows the results of magnetic measurements of a representative segment. Figs. 4(*a*) and 4(*b*) show Hall probe data of the second vertical and horizontal field integrals along the undulator before (black) and after (red) pole tuning at a gap of 14 mm. A significant straightening of the second integral is seen. The RMS value is reduced from 96 to 26 T mm^2. At 17.5 GeV, the residual excursion corresponds to about 0.5 µm RMS. Fig. 4(*c*) shows the local K parameter and Fig. 4(*d*) shows the optical phase on the undulator poles, again at a gap of 14 mm. Data of the 246 magnetically active poles are shown. Before tuning, the variation of the local K parameter, as seen in Fig. 4(*c*), leads to a strong variation in the optical phase seen in Fig. 4(*d*). It is reduced by pole tuning from 11.61 to 2.13° RMS.

Fig. 4(*e*) shows the gap dependence of the K parameter (black) and RMS error of the optical phase (blue). The K parameter decreases monotonically starting from 3.9 at the minimum gap of 10 mm. The K parameters were measured with a relative accuracy $\Delta K/K$ of better than $\pm 2 \times 10^{-4}$ and are used for adjustment during FEL operation.

The optical phase error shows a minimum around 14 mm. This gap, the 'tuning gap', is used for pole tuning. The optical

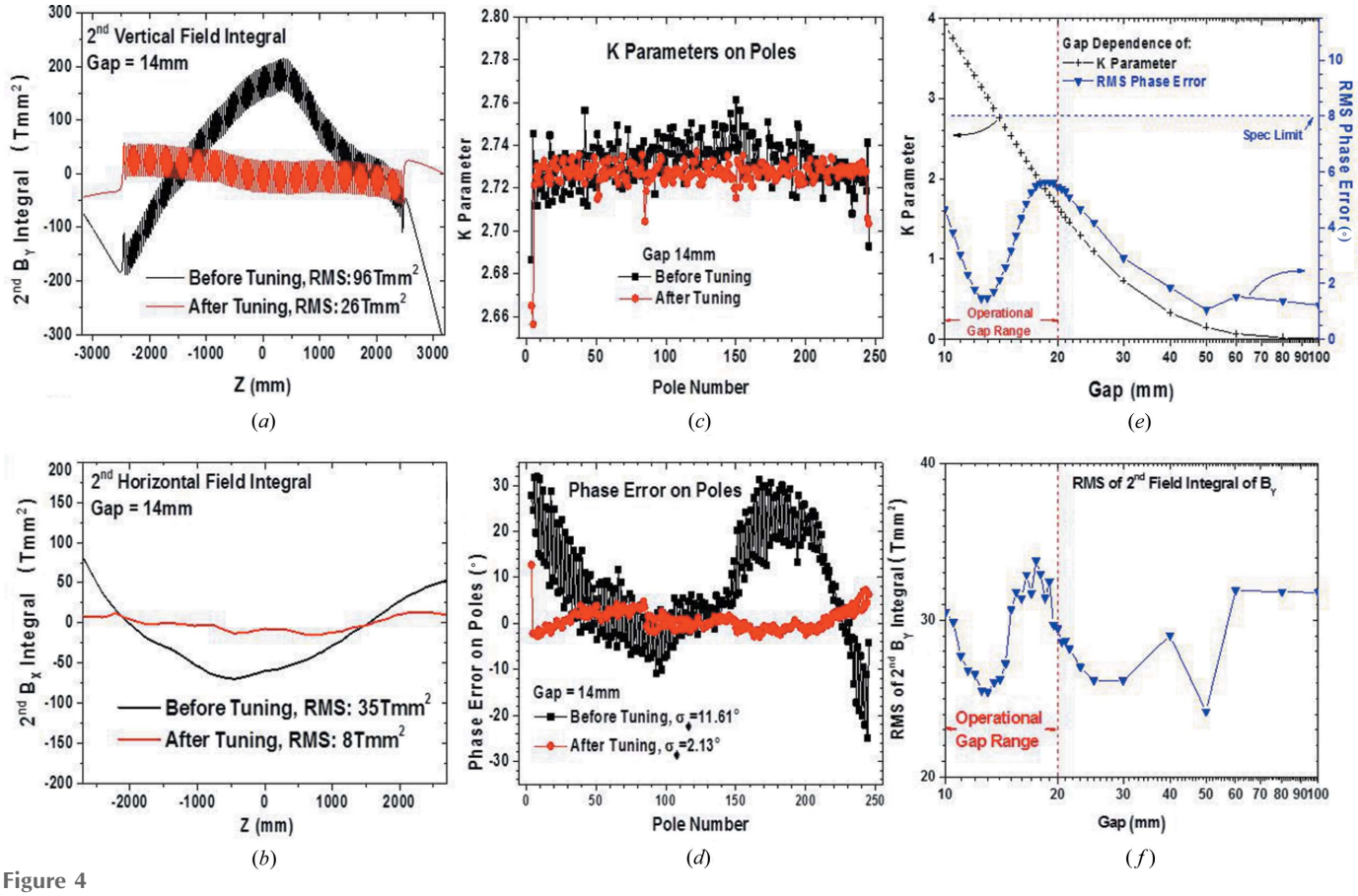

Figure 4
Representative results of magnetic measurements for SASE1 undulator segments. For details, see main text.

phase error is very sensitive to girder deformation resulting from magnetic forces. The changes seen in the phase error in Fig. 4(*e*) reflect the transition from concave deformation at 10 mm gap and 4.5° phase error, to flat at 14 mm with a very small error, to convex at large gaps with about 5.5°. Girder deformation and its effect on phase errors have been observed on all undulator segments and they are well understood (Li *et al.*, 2015). The specification limit of 8° as shown by the dashed line is reliably fulfilled. Finally, in Fig. 4(*f*) the straightness of the trajectory is demonstrated by the RMS of the second vertical field integral. Its maximum is about 37 T mm^2 and again well below specifications. While the operational gap range is 10 to 20 mm, specifications are also fulfilled beyond this limit as well.

2.2. Phase shifters

Phase shifters are needed to control the phase of the radiation emitted by the individual undulator segments so that there is always constructive interference. The required phase adjustment is a function of the *K* parameter, which is determined by the undulator gap. Phase shifters are magnetic elements using NdFeB material and may deflect the beam when their gap is changed. In order to avoid active correctors as for the undulators, first field integral kick errors need to be ±0.004 T mm or less in order to not affect lasing. Therefore, the magnetic design was optimized for low errors and differs from that of undulators. It simultaneously minimizes beam deflection and stray fields. Positive and negative poles are embedded in an iron yoke (Lu *et al.*, 2009). Poles have opposite signs, but they have exactly the same magnetic environment. This symmetry avoids gap-dependent steering errors as long as the material is homogeneous in all magnets. However, magnet inhomogeneities may result in small perturbations, which may require compensation. For this purpose, a precision shimming method has been developed and applied (Li & Pflueger, 2015). Table 2 summarizes the most important phase shifter properties and specifications.

The exact phase matching between two undulators depends on their end fields, which differ between undulators. In order to determine the phase-shifter gap for a specific *K* parameter of the undulator system, a matching strategy was applied (Li & Pflueger, 2017, 2018). Magnetic measurement data of all undulators and phase shifters are used to provide the settings for all phase shifters of a system so that there is the proper phase advance between all undulators.

2.3. Quadrupole movers

For global beam steering the quadrupoles of the intersections can be moved horizontally and vertically by about ±1.5 mm using quadrupole movers, see Fig. 1 (Munilla *et al.*,

Table 2
Specification of the phase shifters for the EuXFEL.

Magnet type	NdFeB hybrid
Period length (mm)	55
Total number of poles	4
Tolerable minimum first field integral error (T mm)	±0.004
Gap range (mm)	10.7–100
Peak field @ minimum gap (T)	1.40
Minimum phase integral @ minimum gap (T^3 mm^2)	22500

2011, 2015). Their horizontal and vertical movement are controlled using absolute linear variable differential transformers (LVDTs) with an accuracy of ±1 µm. There are two advantages of using quadrupole movers: (1) it fits to the footprint of the quadrupole and, therefore, unlike a conventional corrector magnet does not require any additional space so it is a perfect choice for the densely packed intersections; (2) compared with a corrector magnet with an iron core, it is free of any magnetic hysteresis but it has comparable strength. The quadrupole movers are used to adjust the global orbit through the undulator system when all gaps are open to 200 mm.

2.4. Control system

For the control of the undulator system a control system was developed (Karabekyan *et al.*, 2012). It is based on industrial control hardware, using the fast EtherCAT bus for real-time critical communication and an Ethernet network for the exchange of data that are not real-time critical. The system is distributed in the tunnels and the experimental hall. Its main components and subsystems are:

(1) Local control nodes (LCNs). An LCN is the local control system installed, closed by each cell, underneath the ceiling, as seen in Fig. 2. A system like SASE1 contains 35 LCNs. Its central component is a programmable logic controller (PLC) running on an industrial PC, which controls all front-end devices belonging to that undulator cell. These include:

(i) Motion control of the four servo motors and their synchronization with feedback using absolute linear encoders and absolute multi-turn rotary encoders.

(ii) Motion control of the phase shifter with incremental encoder feedback.

(iii) Motion control of the two motors of the quadrupole mover using LVDTs for feedback.

(iv) Control of five power supplies based on lookup tables as a function of the undulator gap: four for the two air coil correctors and one for an ambient field compensation coil, which is integrated in the vacuum chamber.

(v) Recording of the local temperatures at nine different positions distributed throughout the cell.

(vi) Control of a three-way valve for thermal stabilization of the temperature of the undulator vacuum chamber by adjusting the temperature of the cooling water.

(2) Central control node (CCN): this is a central computer, which provides overall control of one undulator system. It is located in the experiment hall. Its tasks are:

(i) Central access point to the hardware of a system. Optical fibre links are used for connecting the CCN with the LCNs in the tunnels. A redundant ring topology is used, which can tolerate a single point failure for the EtherCAT and Ethernet networks. At the beginning and end of a system, there are convertors from optical fibres to copper cables. In between, the individual LCNs are daisy-chained.

(ii) Interface to the distributed object-oriented control system (DOOCS) of the accelerator.

(iii) Communication with external databases to read or save operational data, such as configuration data for the PLCs of the LCNs, gap-dependent lookup tables for K parameter, phase shifter settings, air coil excitation, and other control parameters needed for operation.

(iv) Distribution and installation of new images of operational systems for the PLCs of the LCNs using the image deployment automation (IDA) program. This makes sure that all LCNs of a system run with the same software version.

Fig. 5 shows a schematic diagram of a control system for a EuXFEL undulator system.

The undulator control supports K parameter control of the system. K parameter may be set alternatively in different ways: either by setting a single K parameter for the whole system or any linear/quadratic taper pattern or by a user-defined arbitrary K profile, which can be input externally.

3. Operational experience

3.1. Undulator orbit correction using beam-based alignment

Good overlap between the electron beam and the radiation field is essential for lasing. This requires the electron beam to travel on a straight line over the whole length of the 205 m-long undulator system with an accuracy much better than the FEL beam size of typically 25 µm. This is well beyond the capabilities of conventional alignment methods such as laser trackers. To overcome this limit, the method of beam-based alignment (BBA) was implemented and applied (Emma *et al.*, 1999; Li *et al.*, 2017). With BBA, a straight, dispersion-free (*i.e.* energy independent) global reference orbit through the undulator system is established when all gaps are fully opened to 200 mm. This orbit is kept fixed with high accuracy using the BPMs in the intersections (Lipka *et al.*, 2016). The BBA algorithm moves the quadrupoles using the quadrupole movers in the proper way and gives alignment errors of the quadrupole centres and offsets for BPMs.

Figs. 6(*a*)–6(*c*) illustrate the final results of the BBA (Li *et al.*, 2017). Four different energies, 8, 10, 12 and 14 GeV, were used. Figs. 6(*a*) and 6(*b*) show the vertical and horizontal BPM readings in the 35 undulator cells at these four energies after BBA was performed. It is seen that the readings for different energies coincide very well. They define the new reference orbit. It is seen that, in the horizontal plane, there were deviations from the straight line up to about ±600 µm and, in the vertical plane, up to ±200 µm. These deviations originate from two sources: (1) the accuracy of the referencing of the fiducial marks of the quadrupoles and BPMs leads to offsets of

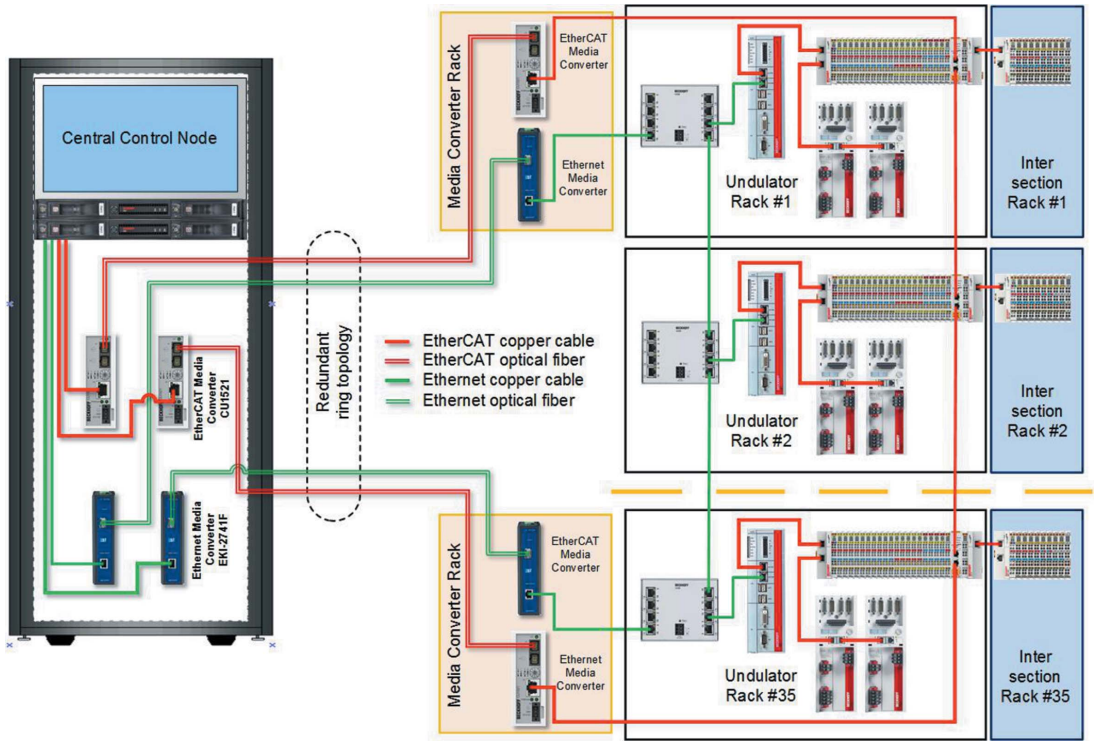

Figure 5
Schematic of a EuXFEL undulator control system.

their nominal centres and is not better than ±50 µm at best, and (2) the accuracy of optical alignment depends on the distance. Over the length of the system of 205 m it is estimated to be ±200–250 µm. The results in Figs. 6(*a*) and 6(*b*) show that, in the horizontal plane, deviations are somewhat larger than this estimate and, in the vertical plane, they seem to be slightly smaller. Nevertheless, the observed deviations were well within the movement range of the quadrupole movers and could be compensated.

Alignment errors for the undulators cannot be measured using BBA but are expected to be on a similar level like the quadrupoles. In the horizontal plane, the undulator poles are 41.7 mm wide so that a 0.6 mm error results in a relative field change of about 10^{-5} and is negligible. The vertical misalignment of up to 0.2 mm may result in a relative field change of the order of up to 5×10^{-4}. If needed, it may be corrected later by retuning the gap or adjusting the middle plane of the undulator. Finally, Fig. 6(*c*) shows the dispersion calculated from the data in Figs. 6(*a*) and 6(*b*).

When the undulator gap is closed, the air coil correctors of the undulator segments are used to correct the field errors of the undulator to keep the orbit stable. To start with, gap-dependent corrector settings were set to zero and the first and second total field integrals were taken from moving-wire measurements made in the magnetic lab (Wolff-Fabris *et al.*, 2016). Thanks to the high resolution of the BPMs, in situ measurements using the EuXFEL electron beam were made to refine the lookup tables. After these corrections, no gap-dependent orbit changes were observed.

In order to reliably achieve lasing, the BBA method is indispensable. Meanwhile, it has been further refined and the measurement time was shortened significantly. A full run with four energies needs a minimum time of about 2 h. At present, it is applied about every two to three months, but, if needed, it might be applied more frequently.

For the optimization of lasing intensity, the air coils and their well tuned lookup tables are needed to facilitate undulator operation.

3.2. Radiation damage

Radiation damage of the permanent magnet material used in undulators is a severe and well known problem leading to degradation of the magnetization of the permanent magnet material. This also applies to X-ray FELs. Just two representative examples are cited (Bizen *et al.*, 2016; Nuhn *et al.*, 2014). The duty cycle of the EuXFEL with its superconducting accelerator is up to 27000 bunches s^{-1} and is two to three orders of magnitude higher than for conventional facilities like SACLA or LCLS I using warm linacs. For EuXFEL this is a severe operational risk. Preventive measures were taken and include a more than 200 m-long dogleg/collimator section in front of the undulator (Balandin *et al.*, 2009) and two beam-loss monitors (BLMs) in every undulator cell (Wamsat *et al.*, 2018), see also Fig. 1. For monitoring the dose exposure of the magnet structures, an online dosimeter system using radiation-sensitive metal-oxide-silicon field-effect transistors (RADFETs) was built and installed (Schmidt-Föhre *et al.*, 2015). Each undulator segment is equipped with a pair of RADFET dosimeters on the top and bottom magnet structure at its upstream entrance side. In addition, in front of each SASE system, there is a so-called diagnostic undulator (DU).

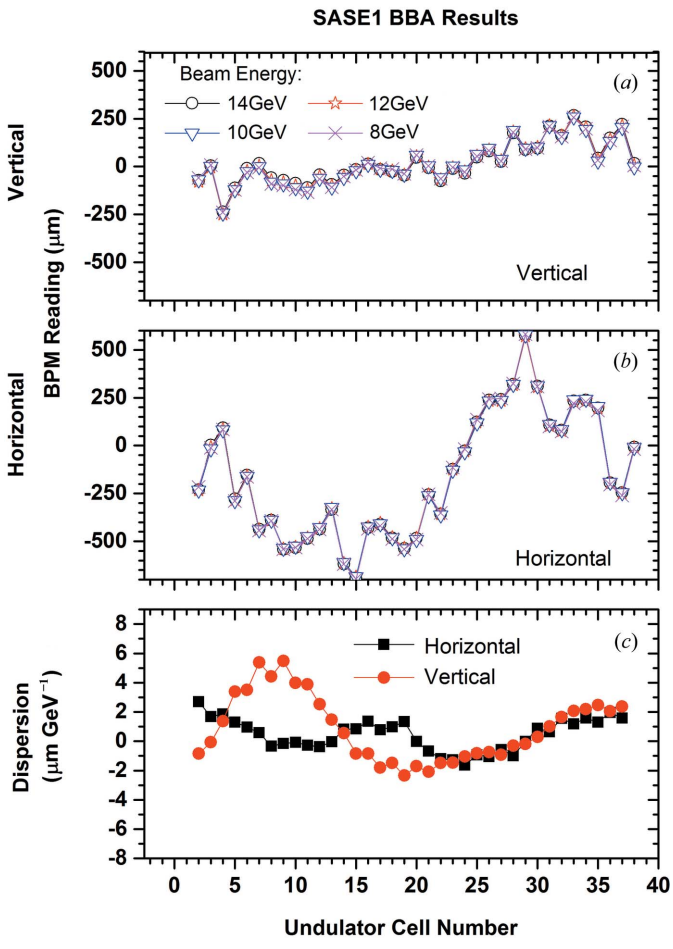

Figure 6
BBA results. (*a*, *b*) Measured offsets of the beam position monitors for four energies, which were used to establish the new baseline. (*c*) Resulting dispersion.

It has the same magnetic parameters as the undulator system but has a fixed gap of 12 mm and a length of only 30 cm. Its weight is about 47 kg. So it can quickly be de-installed and re-installed for frequent re-measurements during a maintenance week. The purpose of a DU is to monitor the degradation of the magnetic properties by radiation exposure.

For all measurements reported in this contribution the EuXFEL was operated at 14 GeV with a bunch charge of 0.25 nC. Repetition rates were up to 5000 bunches s^{-1}. On average 1200 bunches s^{-1} were used.

Fig. 7 shows the total dose along the undulator system measured seamlessly since first beam in April 2017. Initial exposures during first beam and commissioning were quite high. Meanwhile, with increasing operational experience, exposure rates were drastically reduced.

With more than 1000 Gy, the DU, shown in Cell 1, has the highest exposure. Several re-measurements of the DU revealed a degradation rate in the peak field of 0.86% kGy^{-1} (Wolff-Fabris *et al.*, 2018). A tolerable degradation is estimated by the Pierce parameter of $4 \times 10^{-4} = \Delta B/B = \Delta K/K$, resulting in 55 Gy. It is shown by the dashed line in Fig. 7. It is seen that several undulators, especially at the beginning, are

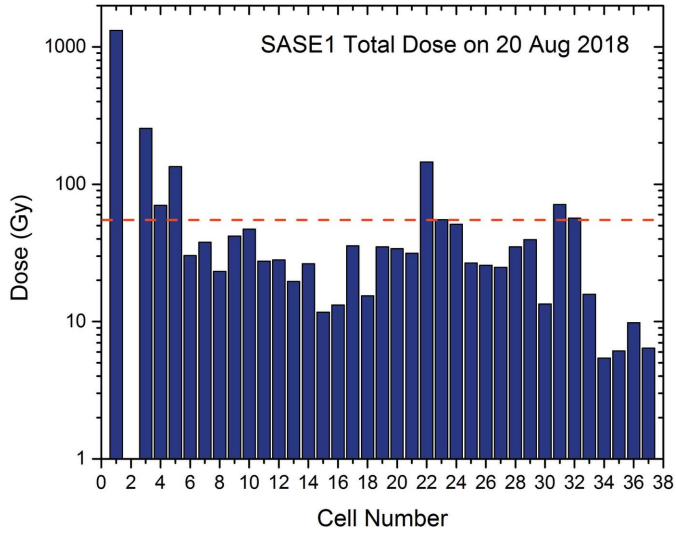

Figure 7
Accumulated dose measured since May 2017. Cell 1 relates to the DU. Undulators start in Cell 3.

already above this level. Therefore, the first one, X069 installed in Cell 3, was de-installed in the winter shutdown of 2017–2018 and re-measured in the magnetic lab. Fig. 8 shows the entrance and exit kicks of the vertical field, B_y, as a function of the gap. The moving-wire method was used (Wolff-Fabris *et al.*, 2016) prior to installation in the tunnel (black) and after the exposure to the measured dose of 230 Gy and de-installation (red). This dose is well above the 55 Gy limit. On the entrance side, Fig. 8(*a*), degradation is clearly seen. It amounts to −0.037 T mm. In contrast, on the exit side, Fig. 8(*b*), no effect is seen at all. In a similar fashion degradation was seen on the peak fields on the poles near the entrance side, Fig. 9. These measurements were made on the EuXFEL Hall probe bench. The relative field reduction of the 22 poles near the entrance side is shown in Fig. 9. Note, the numbering of the 246 active poles of a SASE1 undulator starts from the exit side, so pole 246 is the first. Only the first four poles show degradation. Taking the maximum reduction of -4.70^{-4} T at a peak field of 1.12 T, a reduction ratio of 0.17% kGy^{-1} is estimated, which is about five times smaller than for the DU. The composition of the radiation field leading to the doses shown in Fig. 7 is presently under investigation. Many losses seen in the first cells were caused by mis-steered electrons, especially during accelerator commissioning. Here, with increasing operational experience, already large reductions were observed. In contrast, doses in the middle and end were less dependent on beam conditions. Hard spontaneous undulator radiation plays a role. At 14 GeV, the present energy of EuXFEL, undulator harmonics extend well above 200 keV. In addition, the undulators in the last seven cells were kept open most of the time, which explains the lower doses. So measured radiation doses may be caused by both electron losses and hard photons, but the composition may change along the system and depend on operational conditions. This is supported by neutron-detection measurements. Neutrons could be detected at the beginning of

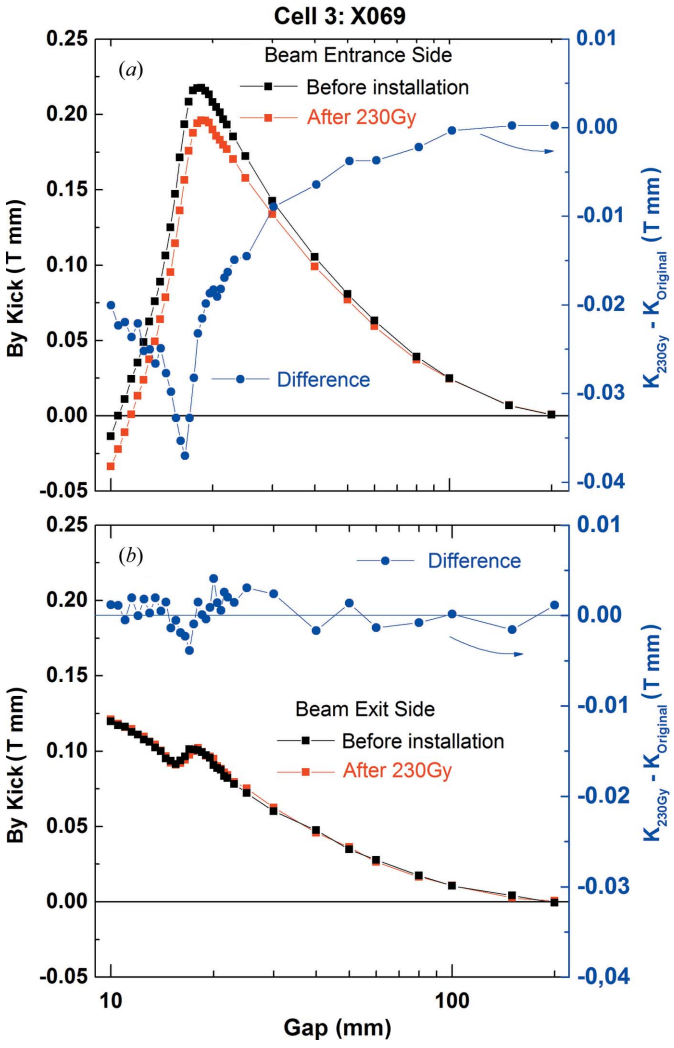

Figure 8
Measured entrance and exit kicks of the first undulator using the moving wire technique. Before installation (black) and after exposure to 230 Gy (red).

the system where they are generated by collisions of high-energy electrons with the vacuum chamber. In contrast, the neutron dose was much lower at the end (Leuschner *et al.*, 2017; Leuschner & Noelle 2018). So some shielding and collimation of the electron beam along the undulator occurs in consistence with the different reduction ratios observed in the DU and the undulator peak fields. While electron impact results in higher radiation damage, as is seen in the DU, pure hard X-rays are expected to have less impact. Irradiation tests of NdFeB magnets showed that within an accuracy level of 0.2%, no damage could be seen for irradiation of 7.4 MGy with 1.3 MeV γ-rays from a ^{60}Co source and 2.4 MGy of bending-magnet radiation from the 7 GeV storage ring of the Advanced Photon Source (Alderman *et al.*, 2002). These doses are three to four orders of magnitude higher than those reported in this paper. However, an ultimate proof of this hypothesis can be given only by re-measurements of undulator segments at different locations of the system after exposure with sufficiently high doses.

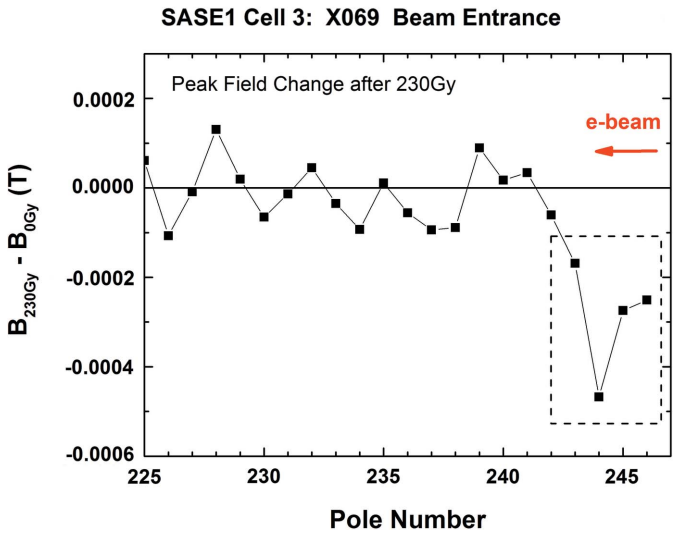

Figure 9
Change of peak fields measured with Hall probe near the entrance side after exposure of 230 Gy. Beam enters from the right. Only the first four poles are affected.

4. Summary and outlook

The design principles and properties of the EuXFEL undulator system were outlined and described. The SASE1 system, the first to become operational, was successfully commissioned and has been in user operation since September 2017.

The overlap of electron beam and laser beam is essential for lasing and was optimized by moving the quadrupoles using the BBA method such that a straight, dispersion-free, electron orbit resulted. BBA, together with the proper tuning and calibration of the undulator and phase-shifter parameters, was essential to obtain lasing reliably with intensities of 1 mJ and more. Meanwhile, BBA has become a standard tool in maintaining lasing properties.

Radiation damage is a great concern not only during first initial commissioning but for long-term routine operation as well. Using the online RADFET system, radiation exposure and its changes can be seamlessly monitored. Significant radiation damage was already observed on the DU and, to a minor extent, on the first undulator segment, where a reduced damage rate was observed. Meanwhile, a great effort was made to optimize beam conditions. This led to a strong reduction in electron beam losses, especially in the DU and the first undulator sections, and was reflected in reduced weekly exposures. There are indications that electron losses occur more in the beginning of the undulator system and, in addition, a significant amount of the measured radiation doses especially towards the end originate from spontaneous radiation of the undulators. Undulator harmonics, which extend well above 200 keV, are believed to cause less damage. For a long-term forecast, however, there are still uncertainties. For the future, therefore, close monitoring and re-measurements of undulators at different positions of the system at doses of 500–1000 Gy or more are planned. This will allow for a more realistic estimate of radiation damage.

Acknowledgements

The authors gratefully appreciate the great help and support by DESY groups MKK1-5, MEA1-3, MVS and all the others during construction and installation. Great thanks to W. Decking, L. Fröhlich R. Kammering, D. Nölle and M. Scholz from the DESY operation team of the EuXFEL for their help and support for the BBA and even more thanks to F. Schmidt-Föhre, D. Nölle and A. Leuschner for the support and interpretation of the radiation-dose measurements.

References

Alderman, J., Job, P. K., Martin, R. C., Simmons, C. M. & Owen, G. D. (2002). *Nucl. Instrum. Methods Phys. Res. A*, **481**, 9–28.

Altarelli, M. *et al.* (2006). Editors. *XFEL: The European X-ray Free-Electron Laser – Technical Design Report*. Hamburg: DESY.

Balandin, V., Brinkmann, R., Decking, W. & Golubeva, N. (2009). *Proceedings of the 23rd Particle Accelerator Conference (PAC09)*, 4–8 May 2009, Vancouver, BC, Canada, pp. 3763–3765. TH6PFP030.

Bizen, T., Kinjo, R., Hasegawa, T., Kagamihata, A., Kida, Y., Seike, T., Watanabe, T., Hara, T., Itoga, T., Asano, Y. & Tanaka, T. (2016). *Sci. Rep.* **6**, 37937.

Dommach, M., Lederer, S. & Lilje, L. (2018). *Vak. Forsch. Prax.* **30**, 47–53.

Emma, P., Carr, R. & Nuhn, H.-D. (1999). *Nucl. Instrum. Methods Phys. Res. A*, **429**, 407–413.

Karabekyan, S., Beckmann, A., Pflueger, J., Burandt, N., Kuhn, J. & Schoeps, A. (2012). *Proceedings of the Third International Particle Accelerator Conference (IPAC2012)*, 20–25 May, New Orleans, LA, USA, pp. 3966–3968. THPPR002.

Leuschner, A., Asano, Y. & Klett, A. (2017). *EPJ Web Conf.* **153**, 08017.

Leuschner, A. & Noelle, D. (2018). Unpublished results.

Li, Y., Abeghyan, S., Berndgen, K., Bagha-Shanjani, M., Deron, G., Englisch, U., Karabekyan, S., Ketenoglu, B., Knoll, M., Wolff-Fabris, F., Viehweger, M., Yakopov, M. & Pflueger, J. (2015). *Synchrotron Radiat. News*, **28**(3), 23–28.

Li, Y., Decking, W. & Scholz, M. (2017). EuXFEL Internal Report WP71/2018/05. In preparation.

Li, Y., Ketenoglu, B. & Pflueger, J. (2015). *Phys. Rev. ST Accel. Beams*, **18**, 060704.

Li, Y. & Pflueger, J. (2015). *Phys. Rev. ST Accel. Beams*, **18**, 030703.

Li, Y. & Pflueger, J. (2017). *Phys. Rev. ST Accel. Beams*, **20**, 020702.

Li, Y. & Pflueger, J. (2018). *Proceedings of the 60th ICFA Advanced Beam Dynamics Workshop on Future Light Sources (FLS2018)*, 5–9 March 2018, Shanghai, China, pp. 103–107. WEP2PT003.

Lipka, D., Affeldt, A., Awwad, R., Baboi, N., Barret, R., Beutner, B., Brinker, F., Decking, W., Delfs, A., Drewitsch, M., Frank, O., Gerth, C., Gharibyan, V., Hensler, O., Hoeptner, M., Holz, M., Knaack, K., Krivan, F., Krouptchenkov, I., Kruse, J., Kube, G., Lemcke, B., Lensch, T., Liebing, J., Limberg, T., Lorbeer, B., Lund-Nielsen, J., Meykopff, S., Michalek, B., Neugebauer, J., Neumann, Re., Neumann, Ru., Noelle, D., Pelzer, M., Petrosyan, G., Pisarov, Z., Pototzki, P., Priebe, G., Rehlich, K., Renner, D., Rybnikov, V., Schlesselmann, G., Schmidt-Foehre, F., Scholz, M., Shi, L., Smirnov, P., Sokolinski, H., Stechmann, C., Steckel, M., Susen, R., Tiessen, H., Vilcins, S., Wamsat, T., Wentowski, N., Werner, M., Wiebers, C., Wilgen, J., Wittenburg, K., Zahn, R., Ziegler, A., Napoly, O., Simon, C., Ignatenko, A., Baldinger, R., Ditter, R., Keil, B., Koprek, W., Kramert, R., Marinkovic, G. M., Roggli, M., Stadler, M., Treyer, D. M. & Kaukher, A. (2016). *Proceedings of the 5th International Beam Instrumentation Conference (IBIC2016)*, 11–15 September 2016, Barcelona, Spain, pp. 14–19. MOBL02.

Lu, H., Li, Y. & Pflueger, J. (2009). *Nucl. Instrum. Methods Phys. Res. A*, **605**, 399–408.

Munilla, J., Calero, J., Cela-Ruiz, J. M., García-Tabaréz, L., Guirao, A., Gutiérrez, J. L., Martínez, de A. T., Molina Marinas, E., Sanz, S., Toral, F., Vázquez, C. (2011). *Proceedings of the Second International Particle Accelerator Conference (IPAC2011)*, 4–9 September 2011, San Sebastian, Spain, pp. 535–537. MOPO026.

Munilla, J., Calero, J., García-Tabaréz, L., Guirao, A., Gutiérrez, J. L., Martínez, de A. T., Molina Marinas, E., Toral, F., Vázquez, C., Martins, C., Ramiro, E., Ramiro, F., Gorrotxategi, J. A., Junkera, B., Tarragual, M., Urzainki, A. (2015). *Proceedings of the Sixth International Particle Accelerator Conference (IPAC2015)*, 3–8 May 2015, Richmond, VA, USA, pp. 2271–2274. TUPWI015.

Nuhn, H.-D., Field, R. C., Mao, S., Levashov, Y., Santana, M., Welch, J. N. & Wolf, Z. (2014). *Proceedings of the 36th International Free Electron Laser Conference (FEL2014)*, 25–29 August 2014, Basel, Switzerland, pp. 127–130. MOP046.

Pflueger, J. (2012). Internal EuXFEL Report WP71/2012/30. Unpublished.

Pflueger, J., Bagha-Shanjani, M., Berndgen, K., Beckmann, A., Biermordt, P., Deron, G., Englisch, U., Karabekyan, S., Ketenoglu, B., Knoll, M., Li, Y., Wolff-Fabris, F. & Yakopov, M. (2013). *Proceedings of the 35th International Free-Electron Laser Conference (FEL2013)*, 26–30 August 2013, New York, USA, pp. 367–371. TUPSO60.

Pflueger, J. & Pannier, R. (2009). Internal EuXFEL Report WP71/2009/01. Unpublished.

Pflueger, J., Lu, H. & Teichmann, T. (1999). *Nucl. Instrum. Methods Phys. Res. A*, **429**, 386–391.

Schmidt-Foehre, F., Froehlich, L., Noelle, D., Susen, R. & Wittenburg, K. (2015). *Proceedings of the 4th International Beam Instrumentation Conference (IBIC2015)*, 13–17 September 2015, Melbourne, Australia, pp. 585–589. WECLA02.

Wamsat, T., Lensch, T. & Smirnov, P. (2018). *Proceedings of the 9th International Particle Accelerator Conference (IPAC2018)*, 29 April–4 May 2018, Vancouver, Canada, pp. 1940–1943. WEPAF053.

Wolff-Fabris, F., Pflueger, J., Schmidt-Föhre, F. & Hellberg, F. (2018). *J. Phys. Conf. Ser.* **1067**, 032025.

Wolff-Fabris, F., Viehweger, M., Li, Y. & Pflüger, J. (2016). *Nucl. Instrum. Methods Phys. Res. A*, **833**, 54–60.